Materials Advances

ROYAL SOCIETY OF CHEMISTRY

PAPER

View Article Online
View Journal | View Issue

Cite this: *Mater. Adv.*, 2025, 6, 2967

Effect of monomer composition on the formation of hybrid polymer-liquid electrolytes for lithium-ion batteries†

Samuel Emilsson, ‡ Gabriele Maffeis,‡ Martina Cattaruzza and Mats Johansson *

Received 11th February 2025,
Accepted 10th April 2025

DOI: 10.1039/d5ma00125k

rsc.li/materials-advances

The electrolyte plays a key role in the performance of novel lithium-ion battery concepts. Hybrid polymer-liquid electrolytes (HEs) are suitable candidates for novel concepts of lithium-ion batteries (LIBs) and lithium-metal batteries (LMBs), where high ionic conductivity coupled with mechanical integrity are required at the same time. HEs are produced through polymerization-induced phase separation (PIPS) of a monomer/electrolyte mixture which allows for the formation of a two-phase system where the domains create a bicontinuous structure. Electrochemical performance and thermomechanical behavior can be tailored through several variables *e.g.*, monomer and solvent chemistries, solvent concentration, and curing conditions. The present study is focused on the chemical structure of the monomer where methacrylate and acrylate monomers are compared as homopolymers or copolymers in HEs. The number of ethylene oxide (EO) units in the backbone of the monomers are furthermore analyzed as a structural parameter. The results show that the monomer structure not only affects the electrochemical and thermomechanical properties, but also defines the morphology of the HEs obtained, which can be in the form of a bicontinuous structure, a gel, or a mixture of the two, according to the kinetic and thermodynamic variables affecting the phase separation and the ultimate T_g of the polymer.

1. Introduction

Today, lithium-ion batteries (LIBs) are the most competitive energy storage systems thanks to their high energy density,[1] which makes them the dominating battery technology on the market.[1–3] However, as the demand for batteries continues to increase, LIBs are starting to reach their ceiling in terms of attainable energy density. This has led to a surge of interest in next-generation batteries. This includes batteries with higher energy densities, such as lithium metal batteries (LMBs), but also new concepts like structural batteries[4] in which the batteries are integrated into the load-bearing structure, or flexible batteries for flexible electronics.[5] New electrolyte materials need to enable safe, efficient and durable cycling of batteries. First, the electrolyte must be compatible with the electrodes,[6] where the solid electrolyte interface (SEI) that is created affects the cycling stability.[7] Other important factors are safety and durability issues, *e.g.* flammability and lithium dendrite growth.[8,9] Electrolyte separators with high mechanical integrity are also desired to improve these features.[6]

Next-generation batteries also put additional demands on the electrolyte. Structural LIBs, for example, require a multifunctional electrolyte with at least 100 MPa storage modulus and 10^{-4} S cm^{-1} ionic conductivity.[10] Liquid electrolytes (LEs) and gel polymer electrolytes (GPEs) are not suitable for this purpose because they do not ensure the stiffness required, while solid polymer electrolytes (SPEs) generally have too low ionic conductivities at ambient temperature.[10–12]

One novel concept is represented by hybrid polymer-liquid electrolytes (HEs), which feature a bicontinuous structure with two phases, a solid polymer network and a liquid that percolates the porous polymer phase.[13] Unlike GPEs, HEs exhibit a higher storage modulus while retaining a sufficient ionic conductivity, at least within the variety of HEs that have been reported so far in the literature.[10,12,13] Furthermore, this bicontinuous structure can be formed *in situ*, infused into the battery assembly.[14]

HEs are obtained through polymerization-induced phase separation (PIPS), which exploits the decreasing solubility of the forming polymer compared to the monomers in the solvent[12,15,16] The obtained morphology of the porous system depends on the chemical composition and polymerization mechanism/conditions.[17,18]

Department of Fibre & Polymer Technology, Division of Coating Technology, KTH Royal Institute of Technology, SE-100 44 Stockholm, Sweden.
E-mail: matskg@kth.se

† Electronic supplementary information (ESI) available. See DOI: https://doi.org/10.1039/d5ma00125k

‡ These authors contributed equally and should be regarded as co-first authors.

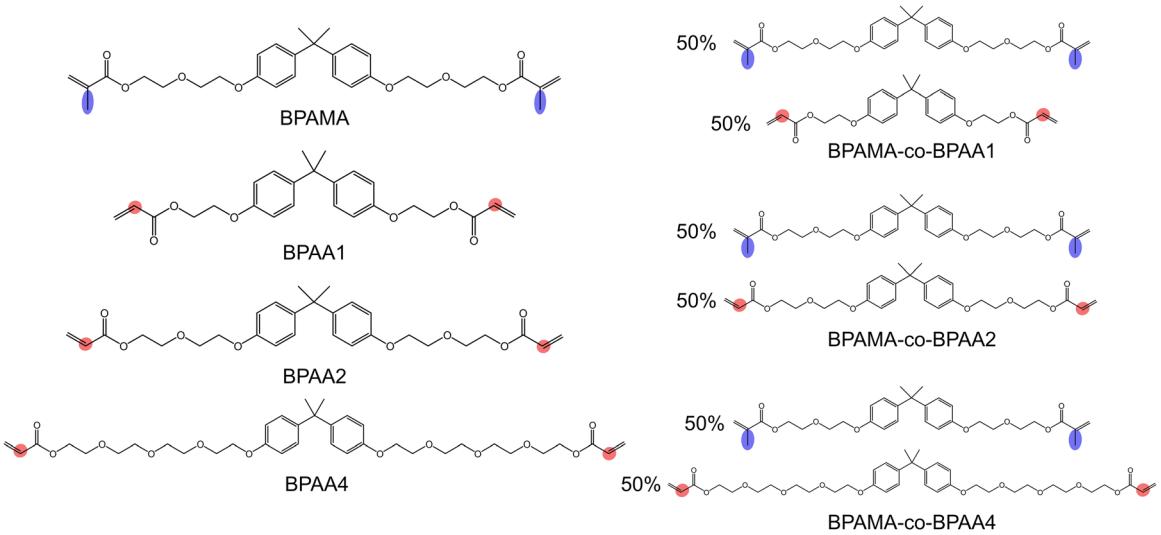

Fig. 1 Chemical structures of all the monomers used for the synthesis of HEs.

PIPS was initially developed for chromatography media, which led to fundamental investigations of the PIPS process. Multiple important works[17,19–21] showed the effect of solvent choice, monomer choice, and polymerization method. These factors have also extensively been reviewed.[15,21–23]

For battery applications, several systems have been explored. Epoxy resins combined with ionic liquids for structural supercapacitor applications.[18,24–26] The effect of monomer structure, solvent and salt concentration have also been investigated for these systems. HEs based on methacrylate monomers and carbonate solvent electrolytes have also been extensively explored showing the effect of monomer structure[14,27] and electrolyte content.[27] The effect of solvent molecular weight[28] and composition[29] has also been studied.

To summarize, a complex interplay of these factors affects the PIPS process, which in turn have a large effect on the properties of the obtained HEs. An ideal HE has pores of sufficient size that allow adequate ionic conductivity, while too large pores lead to a brittle material with insufficient stability.[29,30] The choice of the monomer affects the mechanical properties of the polymer phase, but also how pores are formed during PIPS. The solvent and salt choice affect the electrochemical performance of the liquid phase, while also governing pore formation. All these factors need to be considered when developing new HEs based on PIPS.

The present study aims to relate how the chemical structure of the monomers and curing mechanism affect the final morphology and HE properties. Three variables are investigated, *i.e.*, methacrylate *versus* acrylate monomers, ethoxylate unit content, and homo-*versus* copolymers (see Fig. 1). The properties investigated are conversion, reaction rate, pore size, ionic conductivity, storage modulus, and glass transition temperature (T_g).

2. Experimental

2.1. Materials

Bisphenol A ethoxylate (EO = 2) dimethacrylate (**BPAMA**) (M_n = 540 g mol^{-1}) was donated by Alkema, while bisphenol A ethoxylate (EO = 1) diacrylate (**BPAA1**) (M_n = 424 g mol^{-1}, stabilized with 750 ppm 4-methoxyphenol (MeHQ)), bisphenol A ethoxylate (EO = 2) diacrylate (**BPAA2**) (M_n = 510 g mol^{-1}) and bisphenol A ethoxylate (EO = 4) diacrylate (**BPAA4**) (M_n = 688 g mol^{-1}, stabilized with 250 ppm MeHQ) were provided by Sigma Aldrich. The initiator 2,2′-azobisisobutyronitrile (AIBN) was purchased from Sigma Aldrich, with purity >98%. Ethylene carbonate (EC), propylene carbonate (PC) and lithium trifluoromethanesulphonate imide (LiTFSI) were purchased from Sigma Aldrich. All the compounds were used as received, without any further purification.

2.2. Synthesis

A total of seven different HEs were synthesized with the denotation and compositions presented in Table S1 in the ESI† and illustrated in Fig. 1. Pure polymer samples were also synthesized (*i.e.* without the presence of EC, PC and LiTFSI) in order to study the bulk properties of the respective polymers and are denoted with a "*p*" prior to the sample formulation name.

The synthesis of the different HE formulations was conducted in a glovebox under inert argon atmosphere (<5 ppm O_2) in dry conditions (<5 ppm H_2O). The formulation was prepared by mixing EC and PC in equal volume fractions, with EC being heated at 60 °C upon complete melting. LiTFSI was dissolved into the mixture at 1 M concentration. The formulation consisted of 55 wt% monomer, 45 wt% solvent, and 1 wt% AIBN with respect to the monomer weight. The electrolyte was injected into aluminum molds 30 mm long, 6 mm wide and 0.5 mm thick, covered with a glass plate and clamped at the edges. The structure was sealed into a pouch bag and transferred from the glovebox to the preheated oven, where the curing reaction was performed for 45 minutes at 90 °C. The pure polymers were instead polymerized outside the glovebox at the same curing conditions.

2.3. Electrochemical impedance spectroscopy (EIS)

The evaluation of the ionic conductivity was performed by a Gamry Series G 750 potentiostat/galvanostat/ZRA interface

connected to a four-point resistance setup, with golden electrodes (two reference electrodes 5 mm apart and two working electrodes 20 mm apart). The frequency range chosen was between 300 kHz and 1 Hz. The ionic conductivity was derived from the resistance and the geometrical parameters through Ohm's first law, given by eqn (1), where l is the distance between the reference electrodes, A the cross-sectional area and R_b the resistance measured by the software as the low-frequency intercept on the real axis in the resulting Nyquist plot.

$$\sigma = l/(A \cdot R_b) \quad (1)$$

The cross-sectional area is given by the product of width and thickness of the samples. The width is measured by a digital slide caliper, while the thickness by a thickness gauge. At least one sample from two different batches was tested to ensure reproducibility.

2.4. Fourier-transformation infrared spectroscopy (FTIR)

FTIR analysis was executed to follow the curing performance using a PerkinElmer spectrum 100 FTIR spectrometer equipped with a deuterated triglycine sulfate detector and the golden gate diamond (Specac Ltd) attenuated total reflectance (ATR) accessory and acquired data processed using PerkinElmer Spectrum software. Two samples of each formulation were analyzed both before and after curing. Eight scans per sample were integrated in one spectrum with a resolution of 4 cm^{-1}. Curing performance was evaluated by comparing the area underneath the vinyl peak in the range between 1627–1647 cm^{-1}.

2.5. Real time FTIR

The polymerization rate of all formulations was studied using real time FTIR at atmospheric conditions, *i.e.*, outside the glovebox. Real time FTIR analysis was performed by the PerkinElmer spectrum 100 FTIR Spectrometer equipped with a deuterated triglycine sulfate detector and the golden gate diamond (Specac Ltd) attenuated total reflectance (ATR) accessory and evaluated using PerkinElmer Spectrum software. The plate was pre-heated at 90 °C before the resin was spread on top of the crystal and covered with a microscope slide. The peak area underneath the FTIR spectra between 1627 and 1647 cm^{-1} was measured and the depletion of the signal with time was evaluated. The conversion was calculated through eqn (2), where $C_{\%}$ is the conversion percent and A_0 and A is the area underneath the peak in the range 1627–1647 cm^{-1}, before and after the measurement, respectively.

$$C_{\%} = 100\ (1 - A/A_0) \quad (2)$$

The scanning process proceeded for 15 min and the scans were collected every 5 seconds. Two samples of each formulation were analyzed.

2.6. Dynamic mechanical analysis (DMA)

DMA analysis was performed to determine the thermomechanical properties of the HEs using a DMA Q800 V21.3 Build 96 instrument equipped with an ACS-3 cooling module in tensile film mode. A preload force of 0.125 N was applied and a 1 Hz amplitude strain of 0.1% was used. The clamps were regulated between 10 mm and 15 mm distance from each other before the film was clamped. The temperature was scanned between −50 °C and 200 °C, with a stabilization step for 5 min at −50 °C before the scanning started with a heating rate of 3 °C min^{-1}. The experimental values of T_g were extrapolated from the maximum of the tan δ peak. Wet films (after curing), dried films and pure polymers were tested.

2.7. Scanning electronic microscopy (SEM)

SEM was used to study the morphology of the cross section of dried HEs Before the analysis, the samples underwent 24 h leaching in water and 24 h vacuum drying in an oven at 50 °C in order to extract the liquid electrolyte. Subsequently, the specimens were cryo-fractured through immersion in liquid nitrogen. The cross sections were analyzed by a Hitachi S-4800 microscope equipped with a cold field-emission electron source. The specimens were mounted on an SEM sample holder with conductive carbon tape, and they were subsequently coated with Pt/Pd using a Cressington 208HR sputter coater for 15 s (corresponding to *ca.* 2 nm of the conductive coating layer) at a current of 40 mA. The micrographs were captured with 1 kV accelerating voltage, 10 μA current and 8–9 mm working distance.

2.8. Solvent exclusion

Solvent exclusion was performed to evaluate the percolating structure formation on samples **BPAMA-*co*-BPAA1** and **BPAMA-*co*-BPAA2**. The specimens were soaked into abundant deionized water (>20 mL) and put on a shaking table for 24 h in order to leach the liquid electrolyte out. Subsequently, the samples were dried in a vacuum oven at 50 °C for 24 h and weighed to compare the mass before and after solvent extraction. Two samples of each formulation were analyzed.

3. Results and discussion

BPAMA was chosen as a benchmark since this monomer has been extensively studied previously in the context of polymer-based electrolyte materials. It has been demonstrated to have high thermal and thermomechanical stability, without thermal transitions.[29] In addition, the ionic transport properties like ionic conductivity and transport number of HEs based on **BPAMA** have been studied.[31] Studies have also shown that this monomer can be applied as an HE[32] or separator[29] in half cell configurations as well as structural battery applications,[33,34] showing stable cycling performance.

3.1. The effect of monomer functionality

The termination *via* coupling leads to a faster rise in molecular weight and an earlier gelation point for the acrylates compared to the methacrylates. Moreover, polyacrylates have a significantly lower T_g compared to polymethacrylates.[35,36] This needs to be considered as vitrification effects are possible *i.e.*, if the ultimate T_g is above the curing temperature. The polarity difference between the methacrylates and the acrylates is minor considering the overall size of the monomers.

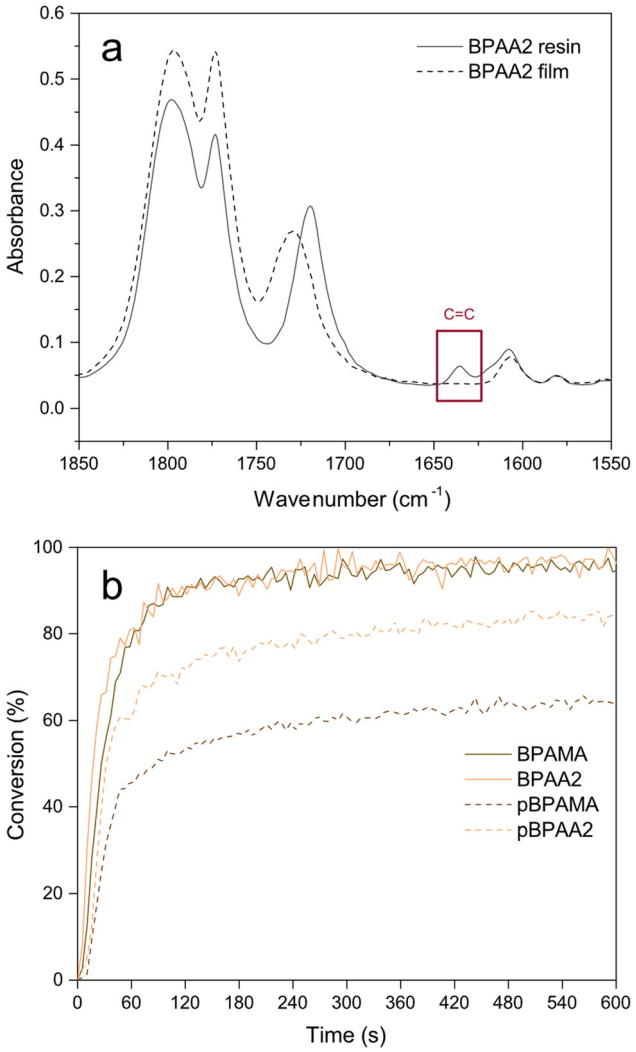

Fig. 2 FTIR spectra before and after curing for sample **BPAA2** (a) and curing performance of **BPAMA** and **BPAA2** as HEs and bulk polymers (b).

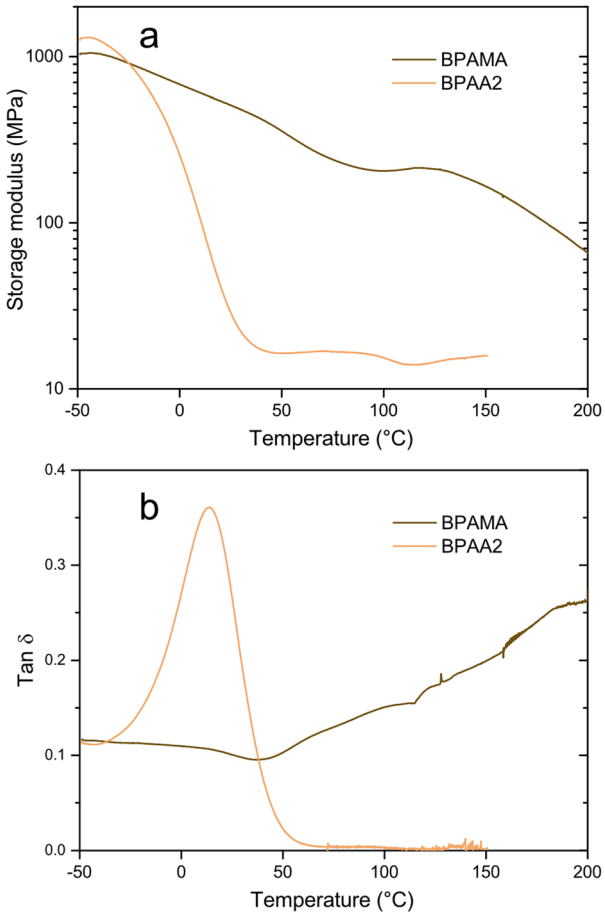

Fig. 3 Storage modulus *versus* temperature (a) and tan δ curve (b) for **BPAMA** and **BPAA2**.

The curing performance of sample **BPAA2** is shown in Fig. 2a, while the others are reported in Fig. S1a–f (ESI†). The shift of the carbonyl peak from 1718 to 1728 is caused by the disappearance of the neighbouring C=C vinyl peak (at 1637 cm^{-1}) during polymerization. The disappearance of this peak was also followed in real-time, to monitor the reaction kinetics. HEs demonstrated to polymerize faster than pure polymers, as shown in Fig. 2b for **BPAMA** and **BPAA2** as examples. The conversion rates for the other polymers are reported in Fig. S2a–e (ESI†). Only minor polymerization rate differences are found among the different HEs since the viscosity of the system and the diffusion limitations are lowered in the presence of the solvent. Moreover, HEs experience a plasticizing effect due to the solvents, which leads to a higher conversion compared to the pure polymer samples. Larger differences are found comparing pBPAMA and pBPAA2 where the reaction depends on the intrinsic properties of the polymer (such as the reaction kinetics and the ultimate T_g), as shown in Fig. 2b. The methacrylate, as expected, polymerized slower and presents a lower conversion due to the intrinsic lower propagation rate and a higher ultimate T_g. The polymerization rate differences are small for all HEs and they all exhibit final double bond conversions above 90%, as shown in Table S2 (ESI†).

Fig. 3a compares the storage modulus of **BPAMA** and **BPAA2**. Although they exhibit similar stiffness in the glassy state (at −50 °C), the modulus of **BPAA2** decreases more rapidly, and it reaches its rubbery plateau at 50 °C. On the other hand, the modulus of **BPAMA** does not decrease as sharply as **BPAA2**, reaching a plateau at 100–150 °C, likely due to the stiffening effect given by solvent evaporation at elevated temperatures. Increasing the temperature further eventually leads to a storage modulus decrease. The storage moduli at 25 °C are listed in Table S3 (ESI†). It should be noted that the resulting storage modulus for **BPAA2** is significantly lower than for **BPAMA**. Moreover, Fig. 3b shows a broad tan δ curve for **BPAMA**, where a peak cannot be recognized, while **BPAA2** has a narrow curve with a clear peak at 14 °C. The differences in Fig. 3 are also corroborated by the differences seen when comparing the pure polymers pBPAMA and pBPAA2 in Fig. S3 (ESI†), which shows that pBPAA2 has a significantly lower T_g compared to pBPAMA.

BPAMA and **BPAA2** have ionic conductivities in the order of 10^{-4} S cm^{-1}. The results obtained are coherent with those

Table 1 Ionic conductivity for homoacrylate HEs

Sample	Ionic conductivity ($\times 10^{-4}$ S cm^{-1})
BPAMA	1.4 ± 0.1
BPAA1	1.3 ± 0.1
BPAA2	1.0 ± 0.1
BPAA4	1.4 ± 0.1

present in the literature.[13] Some minor difference exists between the two HEs (Table 1) which could be ascribed to the morphology as discussed below.

It is expected that the polarity of acrylate compared to the corresponding methacrylate is minor because the methyl group is a small part compared to the bisphenol and EO moieties. Therefore, it can be assumed that the solubility in the polar solvent is comparable between the two species and no dramatic differences should be observed during phase separation and in the final morphology. However, the SEM micrographs of the cross section show a larger porous structure for **BPAMA** compared to **BPAA2** which features smaller pores (Fig. 4). This only gives a qualitative understanding of the porosity, but previous studies have shown a correlation between the size of these structures and a lower tortuosity.[30,31] This is likely the source of the slightly higher ionic conductivity in **BPAMA** compared to **BPAA2**. One explanation to the different porosity is provided by the kinetics of reaction, where acrylates polymerize faster than methacrylates, and have a different termination mechanism.[37] Acrylates also undergo autoacceleration to a larger extent.[38,39] Two other mechanisms can promote or hamper growth after nucleation and depend on the solvent quality[17] and the state of molecular tension of the crosslinked polymer.[21] The ultimate T_g may also play a role, as it may affect the capability of the growing polymer phase to interact with the monomers or solvents. However, a deeper investigation is needed to clarify this aspect.

3.2. The effect of polarity when having the same polymerizable group

As a second parameter, the length of the ethoxy chain was varied (see structures in Fig. 1). The introduction of EO groups makes the monomer more soluble because EO units are slightly polar and interact more with the solvents and salt. Moreover, the length of the spacers is increased, and the aliphatic contribution prevails over the aromatic character. Therefore, the resulting material is expected to be softer. The tan δ curves for homoacrylates are presented in Fig. 5b. Increasing the polarity causes a delay in phase separation, because the oligomer is more soluble in a polar solvent than the oligomer made of the same number of structural units but with less polar functional groups. Hence, the molecular weight of the polymer when phase separation occurs is governed by the solubility.[17] Also, the crosslinking density decreases when the monomer length is extended by adding functional groups. In the present case, the gradual increase in polarity is accompanied with a change in the thermomechanical properties. The T_g and the storage modulus at room temperature decrease because part of the solvent coexists with the crosslinked network in a one-phase system similar to a gel. A gradual decrease in T_g is observed from **BPAA1** to **BPAA2** and **BPAA4**, where the T_gs are 50 °C, 14 °C and −38 °C, respectively. In Fig. 5a, it can be observed that the storage modulus in the glassy state is comparable for **BPAA1** and **BPAA2**, while it is one order of magnitude lower for **BPAA4**, because the formed network is still soluble in the solvent to some extent and phase separation has not occurred completely.

Solvent exclusion indicates the existence of a percolating liquid phase as most of the solvent was extracted after leaching and drying (Table S4, ESI†). A slight difference was observed in **BPAA2**, where 10–15% of the solvent was trapped in the system. Solvent exclusion does not confirm the presence of a bicontinuous structure, unless it is corroborated by SEM micrographs. Indeed, it is illustrated in Fig. 5b that the pore structure size decreases from **BPAA1** to **BPAA2**, and it is absent in **BPAA4**, at least up to ×30.0 k magnitude (Fig. S4, ESI†), assuming that the phase separation partially occurs in **BPAA2** and does not occur in **BPAA4**. All the solvent can be leached out of **BPAA4** because it is one order of magnitude softer than the other HEs at room temperature and therefore facilitates the diffusion of solvent, similar to a gel (Table S4, ESI†). Instead, **BPAA2** is stiffer and retains a fraction of solvent. However, it cannot be concluded whether the morphology of **BPAA2** exhibits a closed porosity or a mixture of bicontinuous and a gel-like structure.

All the samples evaluated in this section belong to the class of acrylates, so they exhibit similar polymerization and termination rates. However, the polarity is highly affected by the introduction or removal of EO units as spacers, that are slightly polar and promote the solubilization into the solvent. The comparison between the acrylates in Table 1 shows that **BPAA1** and **BPAA4** have similar ionic conductivities, while **BPAA2** is around 30% less conductive. DMA and solvent exclusion results, combined with SEM micrographs, prove that the morphology is different for the homoacrylates analysed, and it can be observed that a gradual transition from a bicontinuous system to a gel occurs when the length and solubility of the monomer are increased. Ion transport in HEs is driven by the percolating liquid phase, while in GPEs (with low solvent content) it is dominated by the flexibility of the polymer macromolecules swollen by the solvent.[40] For this combination of solvent and acrylate monomers, it is observed that the ionic conductivity increases when there is a clear prevalence of either the bicontinuous structure or gel, but these mechanisms compete when they coexist. It should be mentioned that a previous study used the BPAAn monomers to develop *in situ*

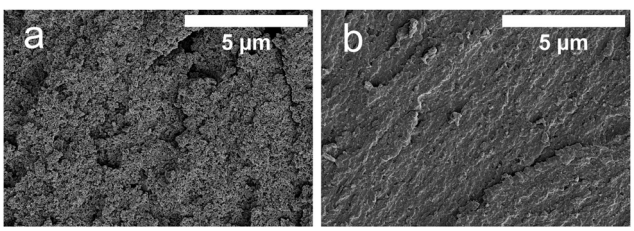

Fig. 4 SEM micrographs of the surface porosity of cross sections for **BPAMA** (a) and **BPAA2** (b).

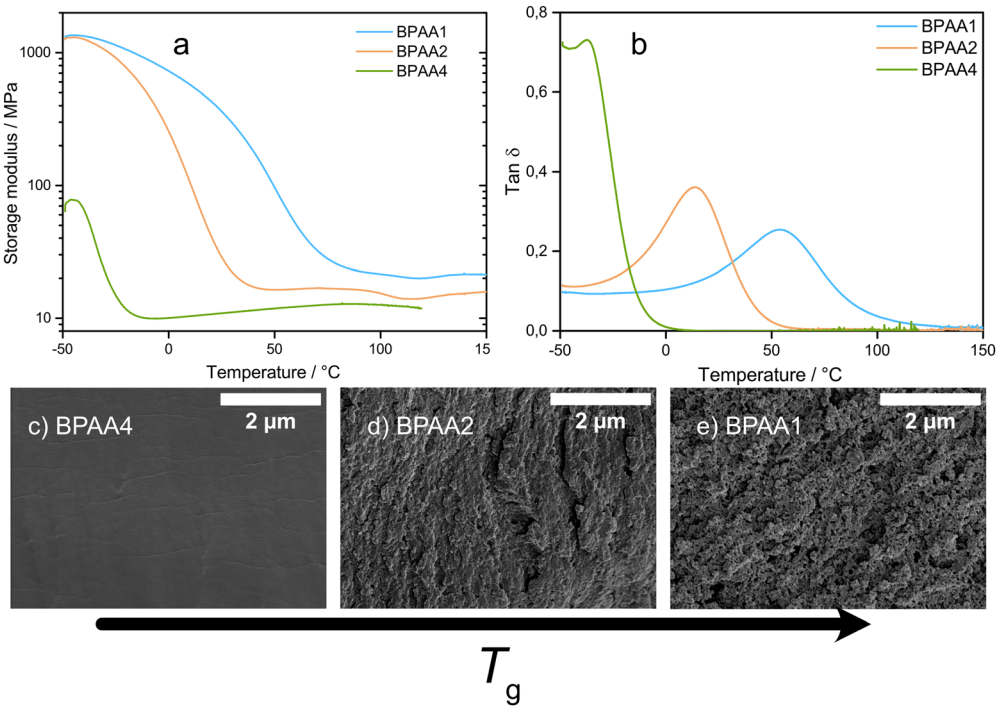

Fig. 5 Storage modulus *versus* temperature (a) and tan δ curve (b) and SEM micrographs of cross sections of (c) **BPAA4**, (d) **BPAA2** and (e) **BPAA4**.

generated GPEs, where the EO units were varied from **BPAA4** to **BPAA15**, all exhibiting the characteristics of a gel, further validating that a transition from a HE to a GPE occurs upon extending the EO chain.[41]

3.3. The effect of copolymerization

By synthesizing copolymers, the PIPS process can be tailored even further to enhance the appreciable electrochemical performance of **BPAMA**. The reactivity ratios of the monomer and the respective polymer give information about the type of copolymer that can be obtained. It has been shown in the literature that methacrylates prefer propagating as homopolymers, contrary to acrylates, that rather copolymerize.[37] This gives that in the first stage the copolymer is richer in methacrylate than expected from the concentration in the solvent, while this deviation is balanced towards higher conversions.

In general, a slow decrease in the storage modulus is combined with a broad tan δ curve. The broadness indicates the presence of a more heterogeneous network structure.[12] Due to the reactivity of the radicals and possible diffusion limitations, intramolecular reactions can take place first, until nanogels are formed,[42] then the reaction proceeds and loose connections are formed between nanogels.[43] The reactivity ratios available for methacrylates and acrylates[37] suggest the intermediate behavior of copolymers. Indeed, DMA results in Fig. 6b underline broad curves for all the copolymers. However, unlike the homoacrylates, a clear T_g cannot be detected due to the broad distribution. The storage moduli represented in Fig. 6a and listed in Table S3 (ESI†) are intermediate between **BPAMA** and the homoacrylates, and they follow the same order as the homoacrylates, where **BPAMA-*co*-BPAA1** is stiffer than **BPAMA-*co*-BPAA2**, while **BPAMA-*co*-BPAA4** is the softest in the whole temperature interval. **BPAMA-*co*-BPAA2** was further analysed to compare the wet/dried HE and pure polymer in Fig. S5 (ESI†). The pure polymer exhibits higher storage modulus than wet/dried HE since the pores create defects in the material. On the other hand, the HE dry films maintain a higher modulus at high temperature. This is likely due to a higher concentration of unreacted monomer in the pure polymer sample acting as a plasticizer.

The ionic conductivities of the HEs based on homopolymers and copolymers are summarized in Fig. 7. Copolymers exhibit improved conductivities compared to the individual components, as proven by **BPAMA-*co*-BPAA2**. By combining the enhanced capability of **BPAMA** to undergo phase separation (Fig. S6a, ESI†), the copolymers benefit from PIPS, as confirmed by the difference in the microstructure between **BPAA4** and **BPAMA-*co*-BPAA4** (Fig. 7c and d), **BPAA2** and **BPAMA-*co*-BPAA2** (Fig. S6b and c, ESI†). **BPAA1** and **BPAMA-*co*-BPAA1** (Fig. 7a and b), instead, show limited differences in the microstructure because **BPAA1** already exhibits pores similar to **BPAMA**. A minimum in ionic conductivity is seen for pure acrylates when EO = 2, while this minimum is not observed in copolymers. For even longer EO chains, also the copolymer could eventually transition into a gel. Although **BPAA4** does not exhibit any porosity (Fig. 7d), it is as conductive as **BPAA1** (Fig. 7b), which clearly contains pores. This confirms that the conduction mechanism for **BPAA4** is based on polymer flexibility typical of GPEs. **BPAMA-*co*-BPAA1** is at least 40% more conductive than the other HEs, meaning that ion transport is promoted by the

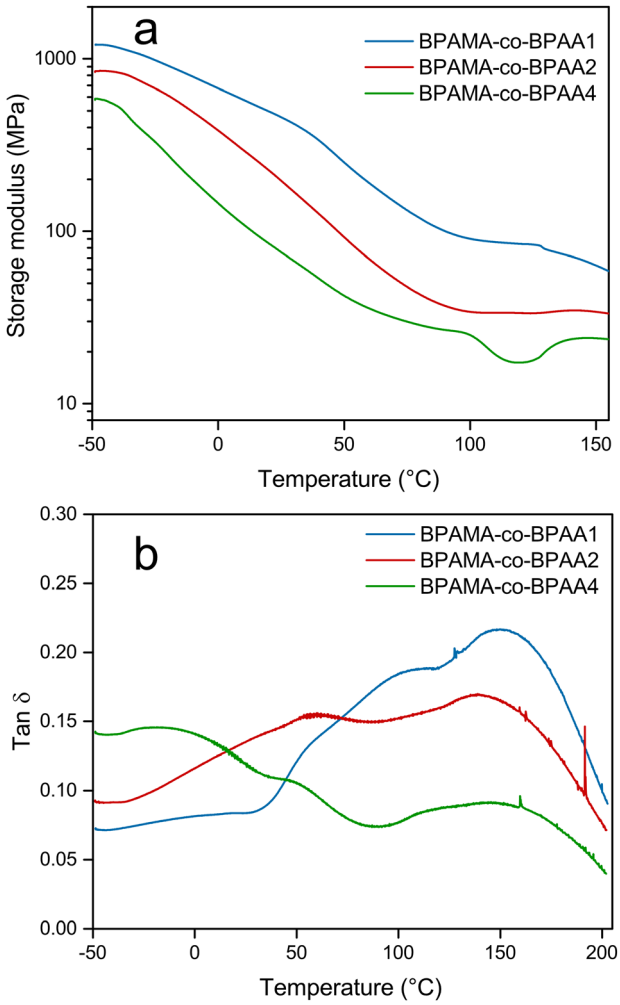

Fig. 6 Storage modulus *versus* temperature (a) and tan δ curve (b) for **BPAMA-*co*-BPAA1**, **BPAMA-*co*-BPAA2** and **BPAMA-*co*-BPAA4**.

high porosity (Fig. 7a). A direct relationship between pore size and opaqueness is underlined when considering the specimens in Fig. S7 (ESI†), because light is scattered in the presence of defects in the material.

4. Conclusions

A number of HEs based on different monomer compositions were synthesized and characterized with respect to their electrochemical and thermomechanical properties, and related to their morphology. It was confirmed that the ionic conductivity is dependent on the average pore size and plasticization of the polymer phase. Homoacrylates have low stiffness at 25 °C, but the respective copolymers, obtained by **BPAMA** and BPAAn 50/50 vol%, show higher thermomechanical stability, and they could in principle be used to replace **BPAMA**. All the HEs exhibited ionic conductivities in the order of 10^{-4} S cm^{-1}, with **BPAMA-*co*-BPAA1** being more conductive than **BPAMA**. A trend can be identified with respect to the monomer structure and composition, where methacrylates promote the formation of pores and subsequent increase in ionic conductivity. The introduction of EO groups reduces the pore formation because solubility is increased. This leads to a transition from HEs to GPEs, having different conductivity mechanisms. Lastly, mixing methacrylate and acrylate monomers is shown to be a route to tailor (optimize) the obtained morphology and properties of the electrolyte systems.

Author contributions

The manuscript was written through contributions of all authors. All authors have given approval to the final version of the manuscript.

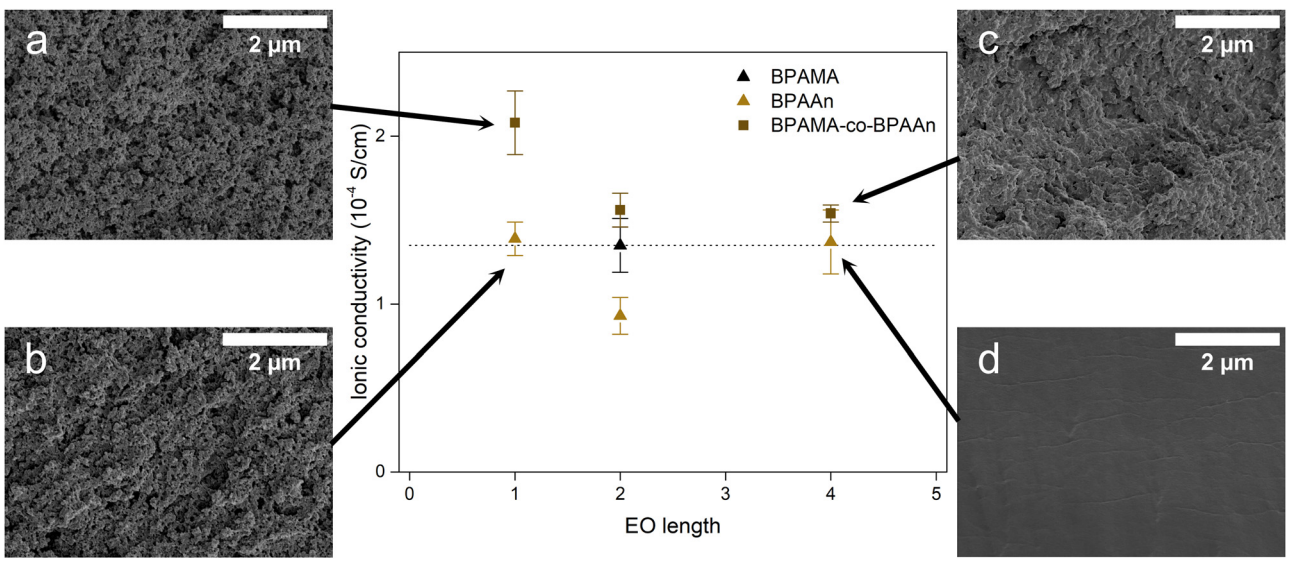

Fig. 7 Ionic conductivity for all the samples considered and micrographs referred to (a) **BPAMA-*co*-BPAA1**, (b) **BPAA1**, (c) **BPAMA-*co*-BPAA4** and (d) **BPAA4**.

Data availability

The data supporting this article have been included as part of the ESI.†

Conflicts of interest

There are no conflicts to declare.

Acknowledgements

KTH Royal Institute of Technology, Polytechnic University of Turin, the Swedish Energy Agency (grant #48488) and Batteries Sweden (BASE) (Vinnova grant: 2019–00064) are gratefully acknowledged for their support.

References

1 T. Placke, R. Kloepsch, S. Dühnen and M. Winter, *J. Solid State Electrochem.*, 2017, **21**, 1939–1964.
2 M. Armand, P. Axmann, D. Bresser, M. Copley, K. Edström, C. Ekberg, D. Guyomard, B. Lestriez, P. Novák, M. Petranikova, W. Porcher, S. Trabesinger, M. Wohlfahrt-Mehrens and H. Zhang, *J. Power Sources*, 2020, **479**, 228708.
3 Y. Nishi, *Chem. Rec.*, 2001, **1**, 406–413.
4 L. E. Asp, M. Johansson, G. Lindbergh, J. Xu and D. Zenkert, *Funct. Compos. Struct.*, 2019, **1**, 042001.
5 Y. Zhao and J. Guo, *InfoMat*, 2020, **2**, 866–878.
6 J. Kalhoff, G. G. Eshetu, D. Bresser and S. Passerini, *ChemSusChem*, 2015, **8**, 2154–2175.
7 K. Xu, *Chem. Rev.*, 2014, **114**, 11503–11618.
8 K. E. Okedu, *Management and Applications of Energy Storage Devices*, BoD–Books on Demand, 2022.
9 X. Q. Xu, X. B. Cheng, F. N. Jiang, S. J. Yang, D. Ren, P. Shi, H. Hsu, H. Yuan, J. Q. Huang, M. Ouyang and Q. Zhang, *SusMat*, 2022, **2**, 435–444.
10 N. Ihrner, W. Johannisson, F. Sieland, D. Zenkert and M. Johansson, *J. Mater. Chem. A*, 2017, **5**, 25652–25659.
11 H. Zhang, S. Kulkarni and S. L. Wunder, *J. Phys. Chem. B*, 2007, **111**, 3583–3590.
12 M. Willgert, M. H. Kjell, E. Jacques, M. Behm, G. Lindbergh and M. Johansson, *Eur. Polym. J.*, 2011, **47**, 2372–2378.
13 M. Cattaruzza, Y. Fang, I. Furó, G. Lindbergh, F. Liu and M. Johansson, *J. Mater. Chem. A*, 2023, **11**, 76–715.
14 N. Ihrner, W. Johannisson, F. Sieland, D. Zenkert and M. Johansson, *J. Mater. Chem. A*, 2017, **5**, 25652–25659.
15 F. Svec, *J. Chromatogr. A*, 2010, **1217**, 902–924.
16 W. Johannisson, N. Ihrner, D. Zenkert, M. Johansson, D. Carlstedt, L. E. Asp and F. Sieland, *Compos. Sci. Technol.*, 2018, **168**, 81–87.
17 C. Viklund, F. Svec, J. M. J. Fréchet and K. Irgum, *Chem. Mater.*, 1996, **8**, 744–750.
18 N. Shirshova, A. Bismarck, S. Carreyette, Q. P. V. Fontana, E. S. Greenhalgh, P. Jacobsson, P. Johansson, M. J. Marczewski, G. Kalinka, A. R. J. Kucernak, J. Scheers, M. S. P. Shaffer, J. H. G. Steinke and M. Wienrich, *J. Mater. Chem. A*, 2013, **1**, 15300.
19 F. Svec and J. M. J. Frechet, *Anal. Chem.*, 1992, **64**, 820–822.
20 H. Minakuchi, K. Nakanishi, N. Soga, N. Ishizuka and N. Tanaka, *Anal. Chem.*, 1996, **68**, 3498–3501.
21 H. M. J. Boots, J. G. Kloosterboer, C. Serbutoviez and F. J. Touwslager, *Macromolecules*, 1996, **29**, 7683–7689.
22 F. Svec, E. C. Peters, D. Sýkora and J. M. J. Fréchet, *J. Chromatogr. A*, 2000, **887**, 3–29.
23 F. Svec and J. M. J. Fréchet, *Science*, 1996, **273**, 205–211.
24 N. Shirshova, A. Bismarck, E. S. Greenhalgh, P. Johansson, G. Kalinka, M. J. Marczewski, M. S. P. Shaffer and M. Wienrich, *J. Phys. Chem. C*, 2014, **118**, 28377–28387.
25 Y. H. Song, T. Kim and U. H. Choi, *Chem. Mater.*, 2020, **32**, 3879–3892.
26 S. J. Kwon, T. Kim, B. M. Jung, S. B. Lee and U. H. Choi, *ACS Appl. Mater. Interfaces*, 2018, **10**, 35108–35117.
27 H. Krebs, L. Yang, N. Shirshova and J. H. G. Steinke, *React. Funct. Polym.*, 2012, **72**, 931–938.
28 S. Emilsson, V. Vijayakumar, J. Mindemark and M. Johansson, *Electrochim. Acta*, 2023, **449**, 142176.
29 S. Emilsson, G. Lindbergh and M. Johansson, *J. Mater. Chem. A*, 2024, **44**, 30442–30453.
30 S. Duan, M. Cattaruzza, V. Tu, R. M. Auenhammer, R. Jänicke, M. K. G. Johansson, F. Liu and L. E. Asp, *Commun. Mater.*, 2023, **4**, 49.
31 M. Cattaruzza, Y. Fang, I. Furó, G. Lindbergh, F. Liu and M. Johansson, *J. Mater. Chem. A*, 2023, **11**, 7006–7015.
32 M. Cattaruzza, M. Johansson, G. Lindbergh and F. Liu, *ChemElectroChem*, 2025, **12**, e202400561.
33 R. Chaudhary, J. Xu, Z. Xia and L. E. Asp, *Adv. Mater.*, 2024, **36**, 2409725.
34 L. E. Asp, K. Bouton, D. Carlstedt, S. Duan, R. Harnden, W. Johannisson, M. Johansen, M. K. G. Johansson, G. Lindbergh, F. Liu, K. Peuvot, L. M. Schneider, J. Xu and D. Zenkert, *Adv. Energy Sustainable Res.*, 2021, **2**, 2000093.
35 L. J. Hughes and G. L. Brown, *J. Appl. Polym. Sci.*, 1961, **5**, 580–588.
36 S. Krause, J. J. Gormley, N. Roman, J. A. Shetter and W. H. Watanabe, *J. Polym. Sci., Part A: Gen. Pap.*, 1965, **3**, 3573–3586.
37 S. Ren, L. Hinojosa-Castellanos, L. Zhang and M. A. Dubé, *Macromol. React. Eng.*, 2017, **11**, 1600050.
38 K. Dusek, *Angew. Chem.*, 1996, **240**, 1–15.
39 G. Odian, *Principles of Polymerization*, John Wiley & Sons, Incorporated, United States, 2004, pp. 464–543, DOI: 10.1002/047147875x.ch6.
40 S. Sen and F. H. Richter, *Adv. Sci.*, 2023, **10**, 2303985.
41 Y. Kang, K. Cheong, K.-A. Noh, C. Lee and D.-Y. Seung, *J. Power Sources*, 2003, **119–121**, 432–437.
42 B. H. Jones, T. M. Alam, S. Lee, M. C. Celina, J. P. Allers, S. Park, L. Chen, E. J. Martinez and J. L. Unangst, *Polymer*, 2020, 205, 122783.
43 S. Seiffert, *Polym. Chem.*, 2017, **8**, 4472–4487.